Electronic Supplementary Information (ESI) for:

3D Printing of Solvent-treated PEDOT:PSS Inks for Electromagnetic Interference Shielding

Saeed Ghaderi[1], Hadi Hosseini[1], Seyyed Arash Haddadi[1], Milad Kamkar[2], Mohammad Arjmand[1,*]

[1]Nanomaterials and Polymer Nanocomposites Laboratory, School of Engineering, University of British Columbia, Kelowna, BC, V1V 1V7, Canada

[2]Department of Chemical Engineering, Waterloo Institute for Nanotechnology, University of Waterloo, 200 University Avenue West, Waterloo, ON, N2L 3G1, Canada

1. Techniques and characterization

Rheology. Rheological measurements were performed using an MCR 102 Anton Paar rheometer (Anton Paar, Austria) equipped with a 25 mm cone and plate geometry with a gap distance of 0.05 mm. Apparent shear viscosity (η) as a function of shear rate ($\dot{\gamma}$) was attained by steady-state flow tests with a logarithmic sweep of the shear rate from 0.01 to 1000 s^{-1}. Dynamic viscoelastic moduli, including storage modulus ($G^{'}$) and loss modulus ($G^{''}$), were measured as a function of shear stress (τ) and shear strain (γ) via dynamic oscillation tests, i.e., strain sweep at a shear frequency of 1 Hz and logarithmic shear stress sweep at a strain of 0.1 %. The printability regions of the different inks were identified based on shear viscosity and dynamic moduli as a function of PEDOT:PSS concentration. All rheological measurements were carried out at 25 °C with a preliminary equilibration time of 45 s.

Topography. The topography of the printed lines and the quality of printing were studied using 3D laser microscopic scanning equipment (Olympus LEXT OLS5000). To achieve the line width and thickness, 20 cross-sectional laser paths were determined for the printed lines for each sample. To be more precise, the maximum width and thickness of each cross-section are considered the line width and thickness values, respectively. To obtain the line surface roughness profile, the laser paths were defined on all printed lines for each sample.

SEM. Tescan Mira 3 XMU Scanning Electron Microscope (SEM) was used to evaluate microscale images of the 10 nm platinum sputter-coated 3D-printed PEDOT:PSS-based structures.

Electrical conductivity. To measure the electrical conductivity, the drop-casted inks on glass slides were dry-annealed and a linear four-point probe (Loresta GP, MCP-T610, Mitsubishi Chemical Co., Japan) set-up was used at the applied voltage of 10 V. The thickness of the formed uniform films on the surface of the glass slides was measured using the same laser microscope set-up. For each sample, the conductivity measurements were repeated three times and the average values were reported as the final conductivity of the sample.

XPS. XPS (Thermo Scientific K-Alpha, USA) was used to achieve the chemical structure of pristine PEDOT:PSS and solvent-treated PEDOT:PSS using a Monochromated Al Ka X-ray source with a nominal spot size of 400 μm. Initial survey spectra of the samples were attained within a pass energy of 200 eV, followed by low-resolution scans of the spectral regions of interest (PE, 150 eV), and finally high-resolution spectra of the main components (PE, 25 eV) for chemical state information. A combined e^-/Ar^+ flood-gun was utilized to supply the charge compensation in the system. Avantage software (Version 5.9925) was employed to process and fit all the achieved XPS data.

XRD. Wide range XRD spectra of pristine, co-solvent doped, and solvent post-treated PEDOT:PSS inks and structures were obtained using (Rigaku ULTIMA III) in conventional 2-theta geometry (3°- 60°), with Cu-K α radiation (λ = 1.5406 Å) at 40 kV and 100 mA. The samples were prepared by drop-casting the inks on clean double-sided silicon wafer substrates and then dried at 140 °C for 2 h. A blank silicon wafer was also tested, and all achieved results were normalized to that of the blank silicon wafer to remove the effects of the substrate.

Raman. Raman spectra were obtained using a Bruker Senterra Raman microscope with a He-Ne laser source at 632.8 nm and ×50 lens (NA = 0.51) and the laser power has always been kept at 0.2 mW to avoid sample degradation.

Mechanical properties of films. The mechanical properties of pure PEDOT:PSS and DMSO-doped 6 wt.% PEDOT:PSS films were evaluated via a Universal Testing Machine (ZwickRoell, Germany) equipped with 200 N load cell in tensile mode at a rate of 1 mm/min.

EMI shielding. EMI shielding performance of the manufactured shields was measured in the X-band frequencies (8.2 GHz to 12.4 GHz) using WR-90 rectangular waveguides and a Keysight P9374A vector network analyzer. The network analyzer sends a single frequency signal from port one (S1) to the sandwich sample, and the receiver detects the reflected (S11) and transmitted (S21) waves along with their phase and magnitude. The same process occurs by port two and the same single frequency signal (S2) is emitted from port two and the reflected (S22) and transmitted (S12) wave is detected by the receiver. Since the frequency and EMI shield for these two measurements are the same, for a uniform and homogenous shield, the magnitude of S11 and S22, as well as S12 and S21 should be equal. Then, the same measurements are repeated for the whole spectrum of the frequencies. The reflection and transmission of the waves were reported as complex scattering (S) parameters. The electromagnetic wave absorption of a shield is defined based on the measured reflectance (R) and transmittance (T), as follows:

$$A = 1 - R - T \tag{1}$$

$$R = \left|\frac{P_R}{P_0}\right| = |S_{11}|^2 = |S_{22}|^2 \tag{2}$$

$$R = \left|\frac{P_T}{P_0}\right| = |S_{12}|^2 = |S_{21}|^2 \tag{3}$$

where P_R, P_T, and P_0 are the power of the reflected, transmitted, and incident wave, respectively. S_{11} is the reflected voltage magnitude over the incident voltage magnitude in port S1, and S_{21} is the transmitted voltage magnitude from port 1 to port 2 over the incident voltage magnitude in port 1. The EMI shielding efficiency is quantified by the EMI shielding effectiveness (EMI SE) of a shield, as shown below:

$$SE_R = 10\log\left(\frac{1}{1-R}\right) = \log\left(\frac{1}{1-|S_{11}|^2}\right) = \log\left(\frac{1}{1-|S_{22}|^2}\right) \tag{4}$$

$$SE_A = 10\log\left(\frac{1-|S_{11}|^2}{|S_{11}|^2}\right) = 10\log\left(\frac{1-|S_{22}|^2}{|S_{21}|^2}\right) = \log\left(\frac{1-R}{T}\right) \tag{5}$$

$$SE_{Total} = SE_R + SE_A \tag{6}$$

2. Rheology and DIW

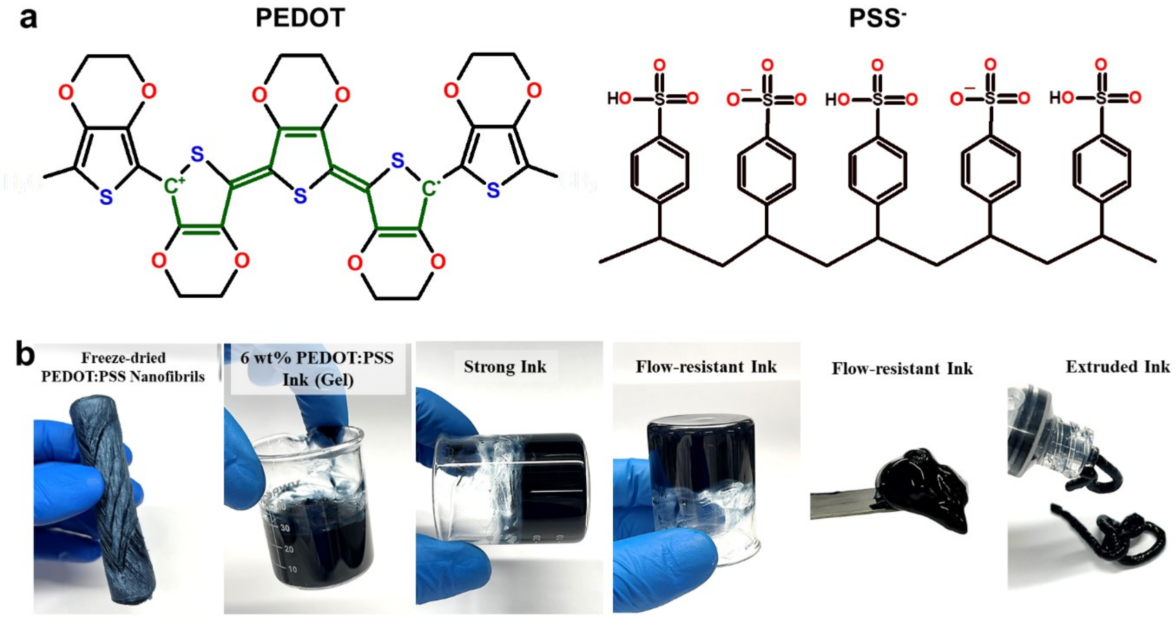

Figure S1. Chemical structure of PEDOT:PSS (a). Freeze-dried PEDOT:PSS nanofibrils and 6 wt.% ink of redispersed freeze-dried PEDOT:PSS nanofibrils in water. The redispersion of high concentrations of PEDOT:PSS in water results in strong flow-resistant inks (gels), which maintain their shape in the free state. These inks are favorable for 3D direct ink writing (b).

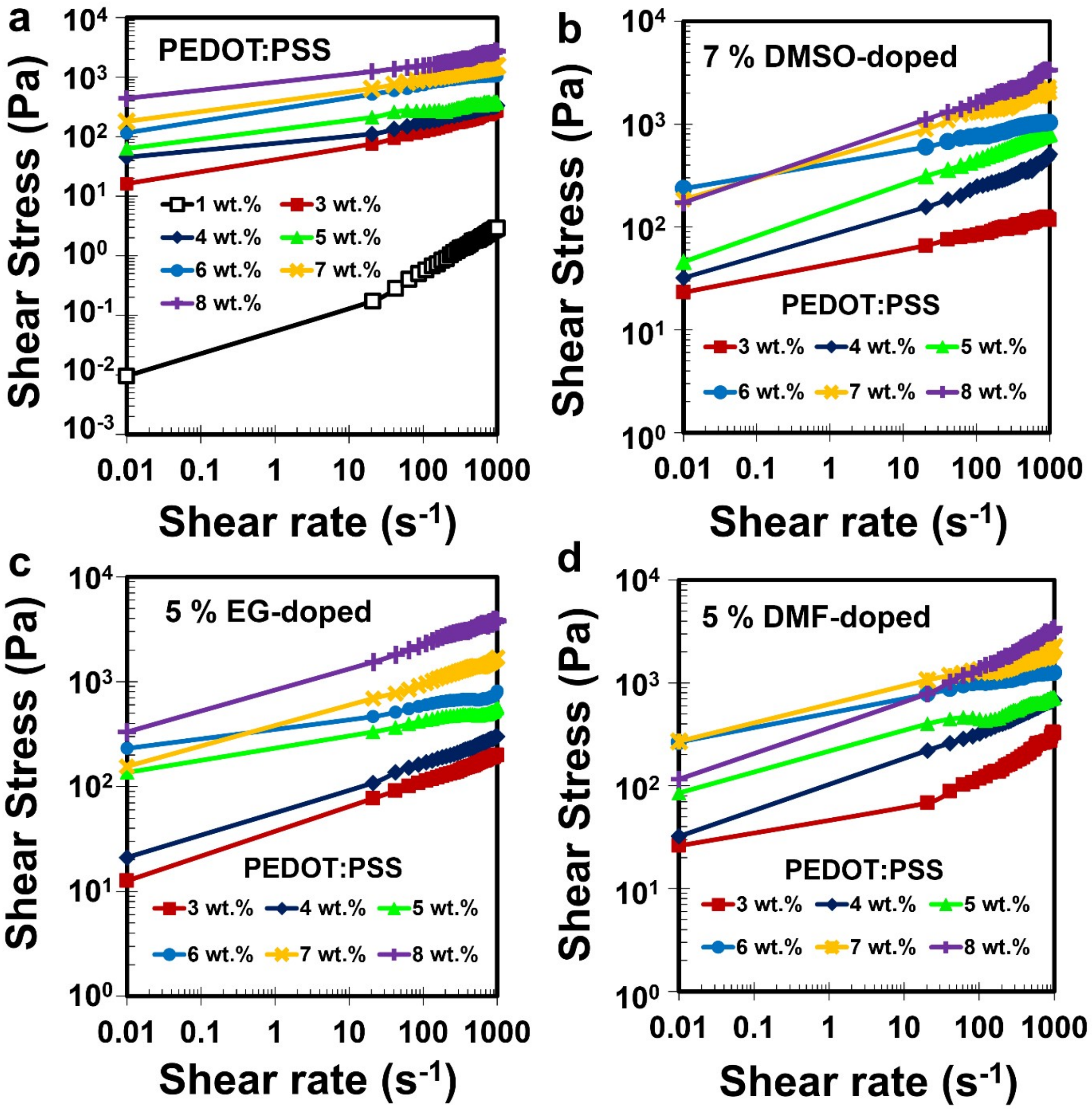

Figure S2. Shear stress-shear rate experimental data for pristine and co-solvent-doped PEDOT:PSS inks.

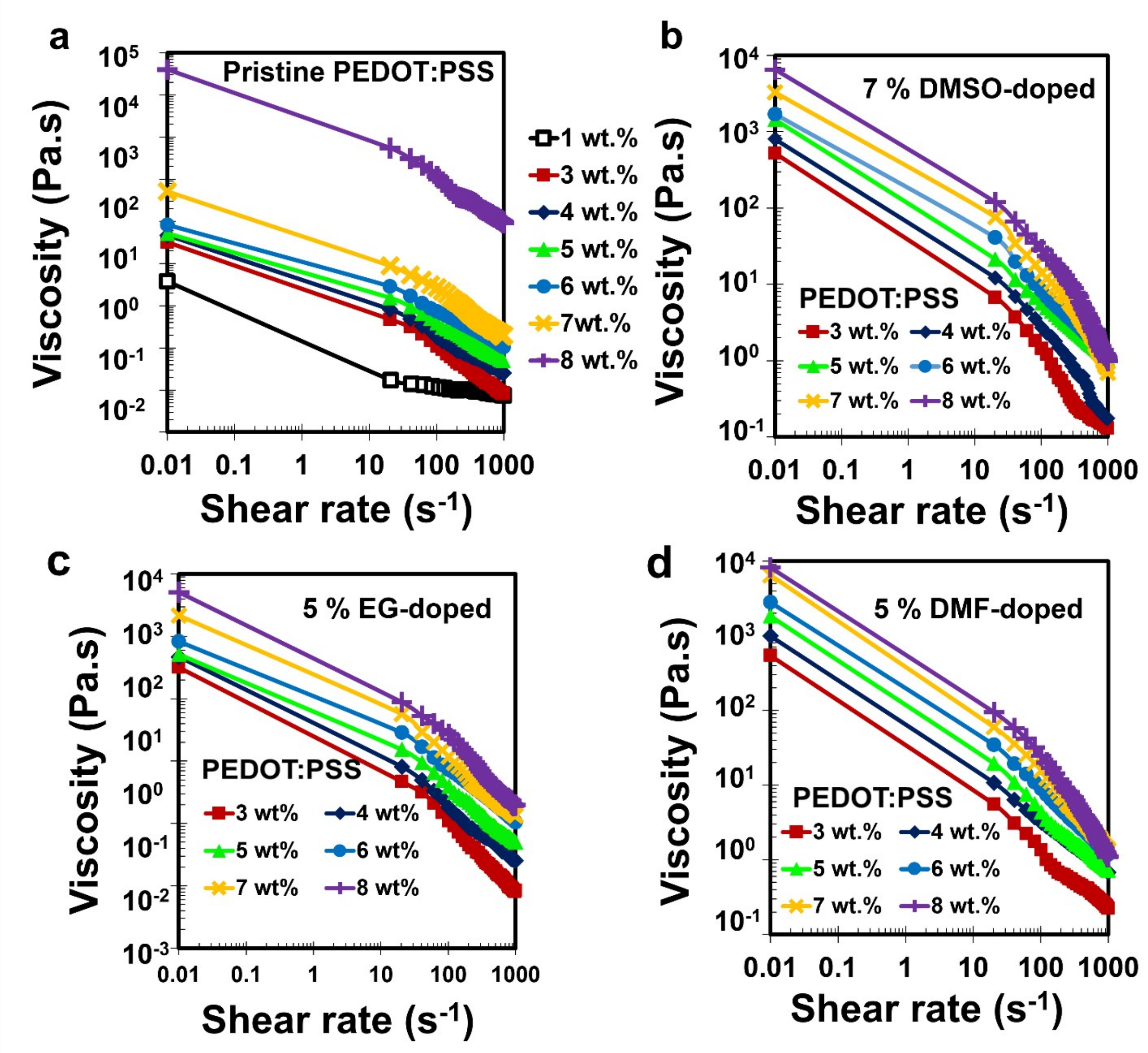

Figure S3. Shear viscosity-shear rate curves of PEDOT:PSS inks with and without co-solvents. The results represent the shear-thinning behavior by increasing the shear rate for all inks. By increasing the concentration of PEDOT:PSS, the shear viscosity increases due to the chain entanglements and forming a 3D physical network. By the addition of co-solvents, the shear viscosities increase due to the interaction of co-solvents polar molecules with the PEDOT:PSS. Additionally, the addition of co-solvents improves the shear-thinning response of the inks.

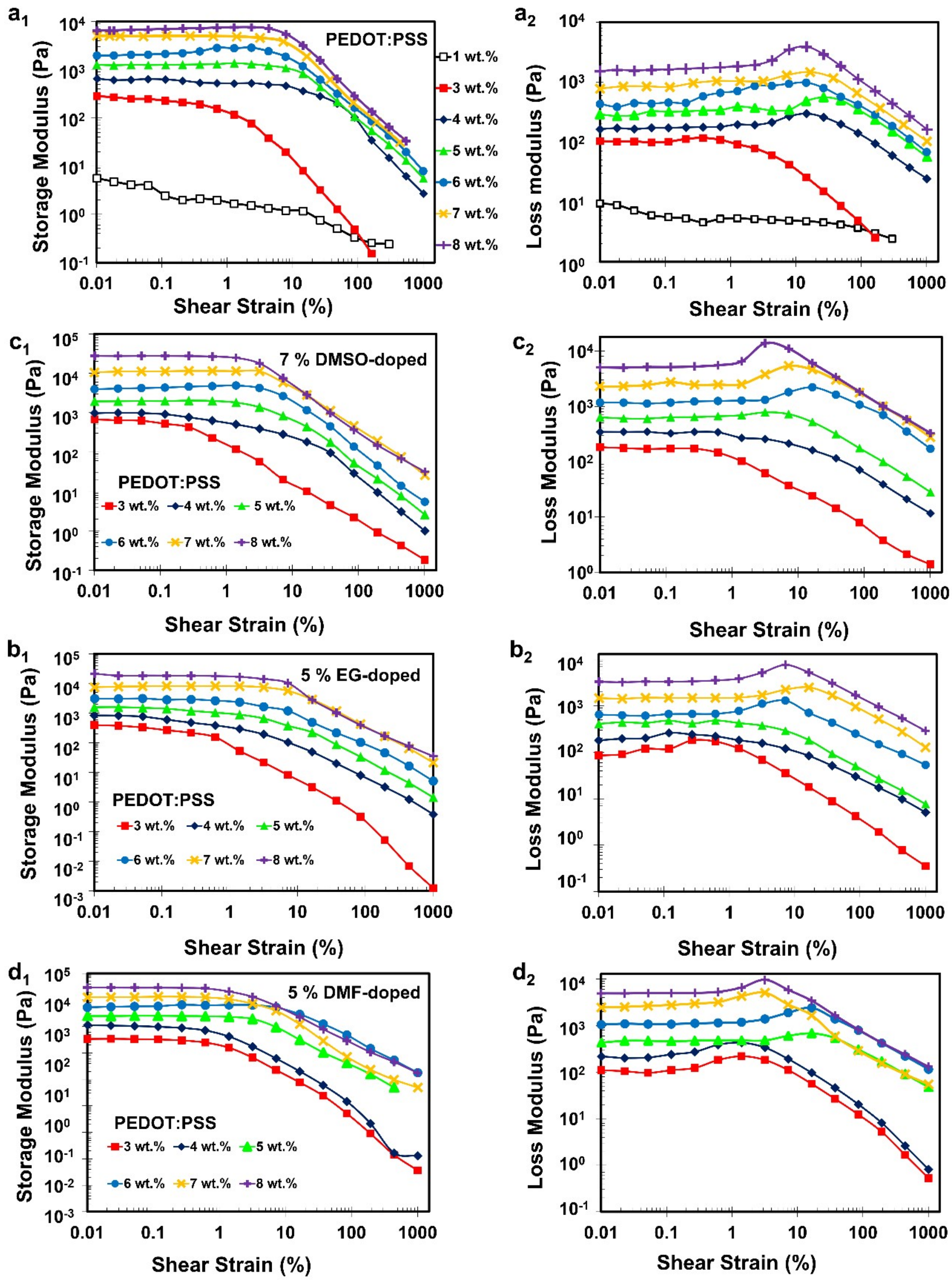

Figure S4. Storage and loss moduli as a function of shear strain for pristine (a_1, a_2), EG-doped (b_1, b_2), DMSO-doped (c_1, c_2), and DMF-doped (d_1, d_2) PEDOT:PSS inks. All the prepared inks show viscoelastic linear region (VLR) at low concentrations (< 1 %). 0.1 % and lower strains can be selected as the VLR for further rheological measurements. The concentration of co-solvents is 7 vol/vol % to water.

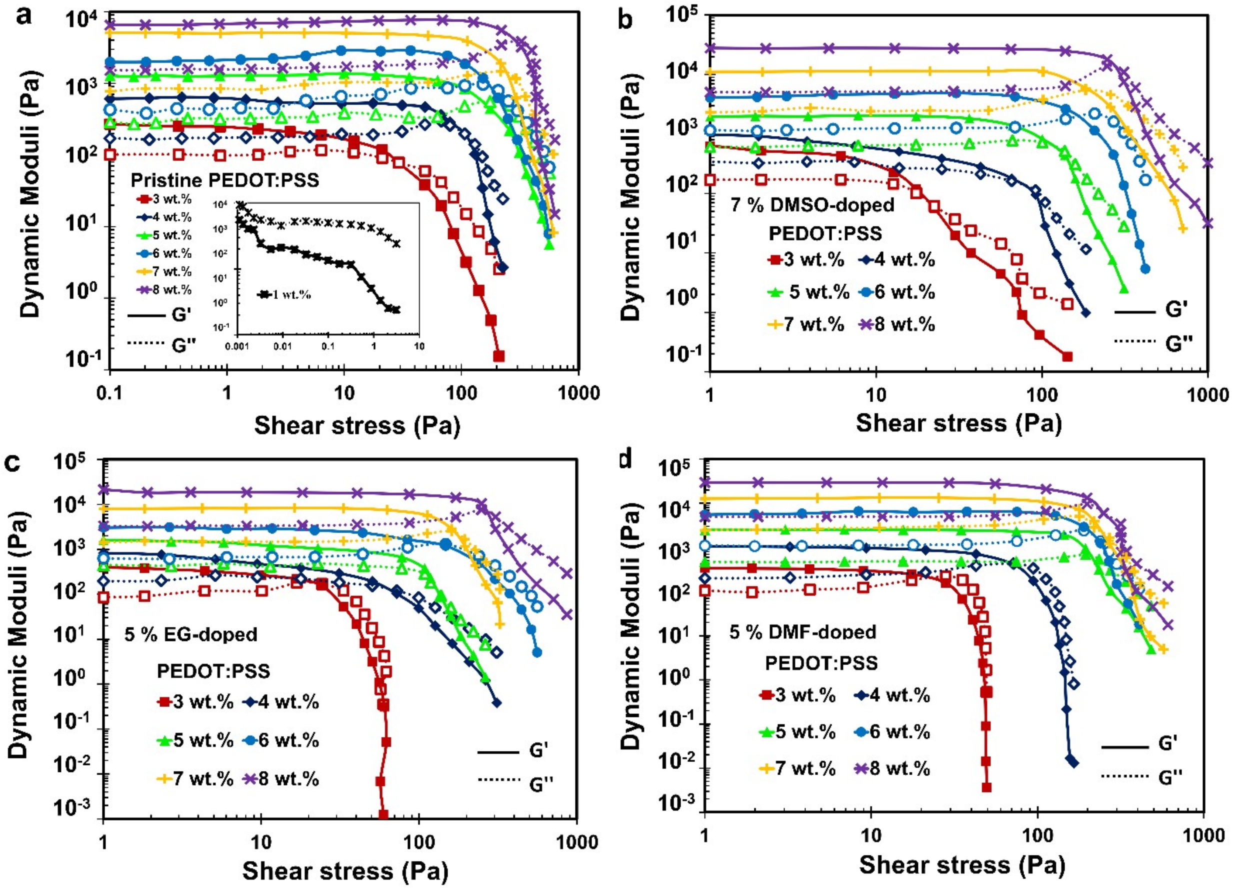

Figure S5. Dynamic moduli-shear stress curves for PEDOT:PSS with and without co-solvents. By increasing the concentration of PEDOT:PSS as well as by the addition of co-solvents, the yield stress (stress at which G′ and G″ curves cross) increases. The shear yield stress is a shear stress at which shear, and loss moduli maintain the same values. The concentration of co-solvents is 7 vol/vol % to water.

The effect of the addition of co-solvent (DMSO) on the mechanical properties of PEDOT:PSS was evaluated in tensile mode, and the results are shown in **Figure S6**. On the basis of tensile testing outcomes, it can be observed that the elongation at break of PEDOT:PSS film decreased dramatically from 0.88 for pristine PEDOT:PSS to 0.57 for DMSO-doped PEDOT:PSS. In this line, DMSO-doped PEDOT:PSS became more brittle compared with pure PEDOT:PSS, as the former experienced a higher Young modulus (E) at 1640 MPa, while the latter presented a value at 958 MPa. It is an expected outcome as the presence of PSS with long chains within PEDOT:PSS contributes to the formation of entanglements. These entanglements play a crucial role in enhancing the elongation of the sample during the tensile test. Upon doping with DMSO, there will be a gap between PSS and PEDOT macromolecules that can adversely impact the elongation of the doped sample. It is worth mentioning that PSS has a long chain compared to PEDOT with significantly shorter chains. As a result, the impact of PSS long chains during the tensile test would be more pronounced.

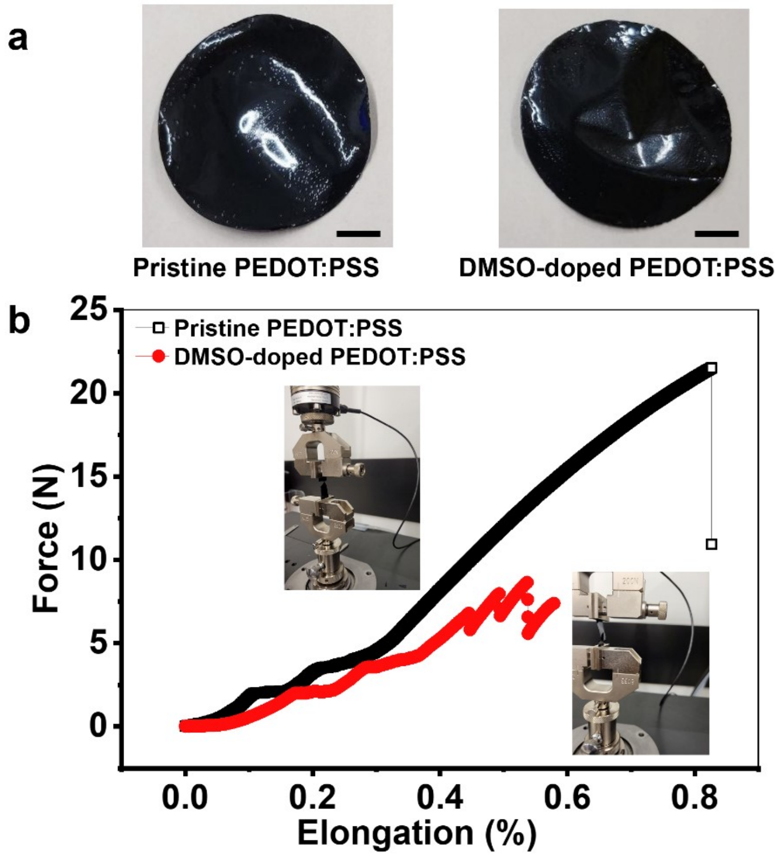

Figure S6. Prepared films of pristine PEDOT:PSS and DMSO-doped PEDOT:PSS (a). Plots of tensile test for pristine PEDOT:PSS and DMSO-doped PEDOT:PSS (b).

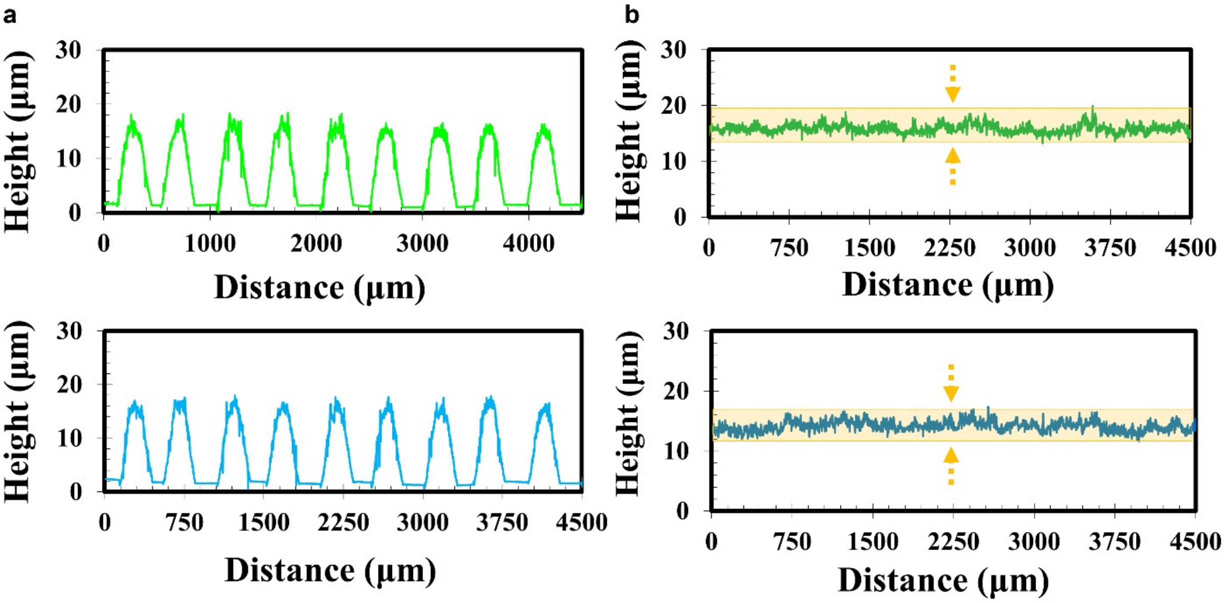

Figure S7. Profile (a) and surface roughness (b) of the printed lines of 6 wt.% PEDOT:PSS doped with 7 vol/vol % DMSO/water ink.

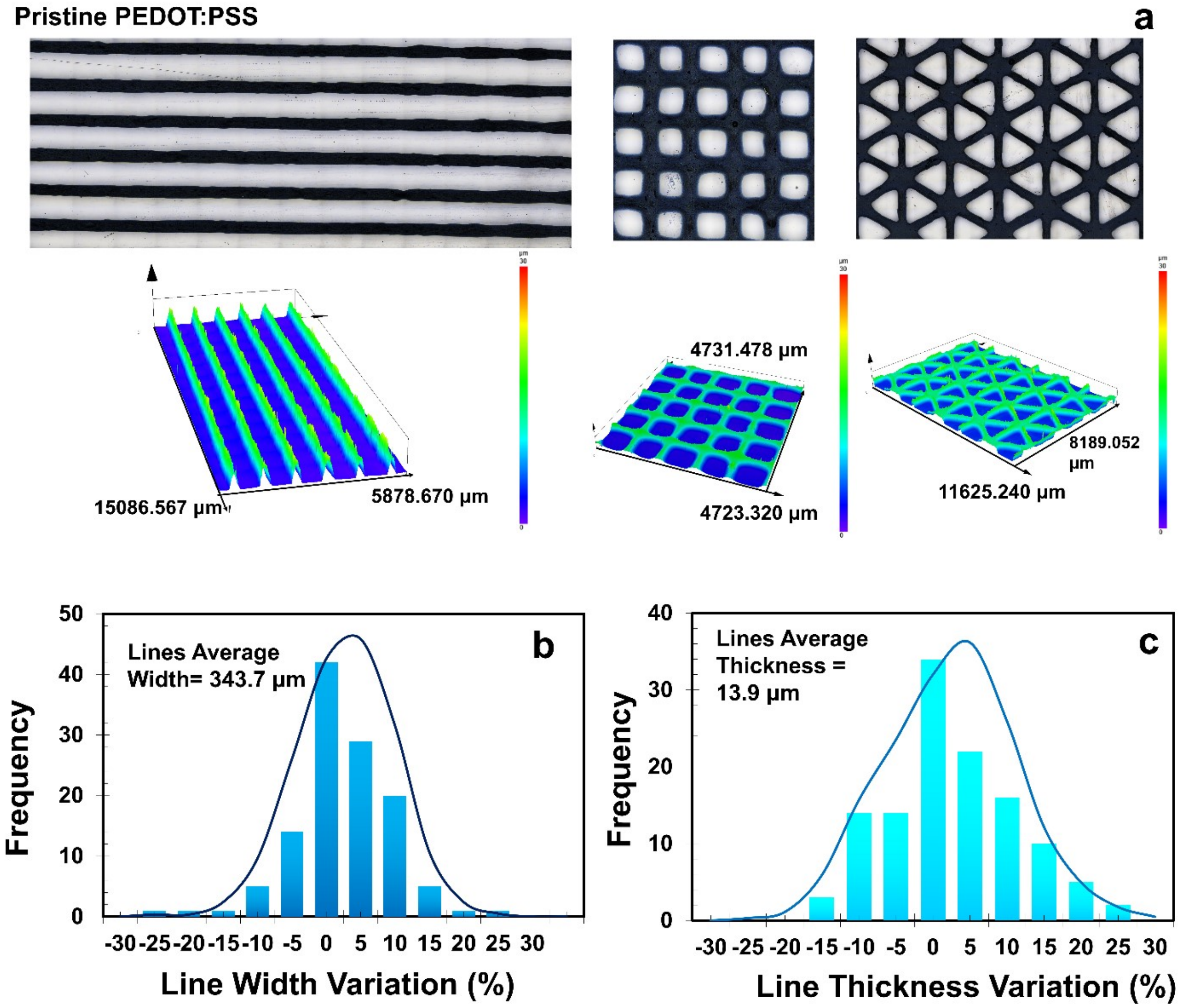

Figure S8. Topographical micrographs of line-, grid-, and triangle-patterned structures of pristine 6 wt.% PEDOT:PSS ink (a), statistical analysis of line width variation (b) and line thickness variation (c) of the printed pristine 6 wt.% PEDOT:PSS lines.

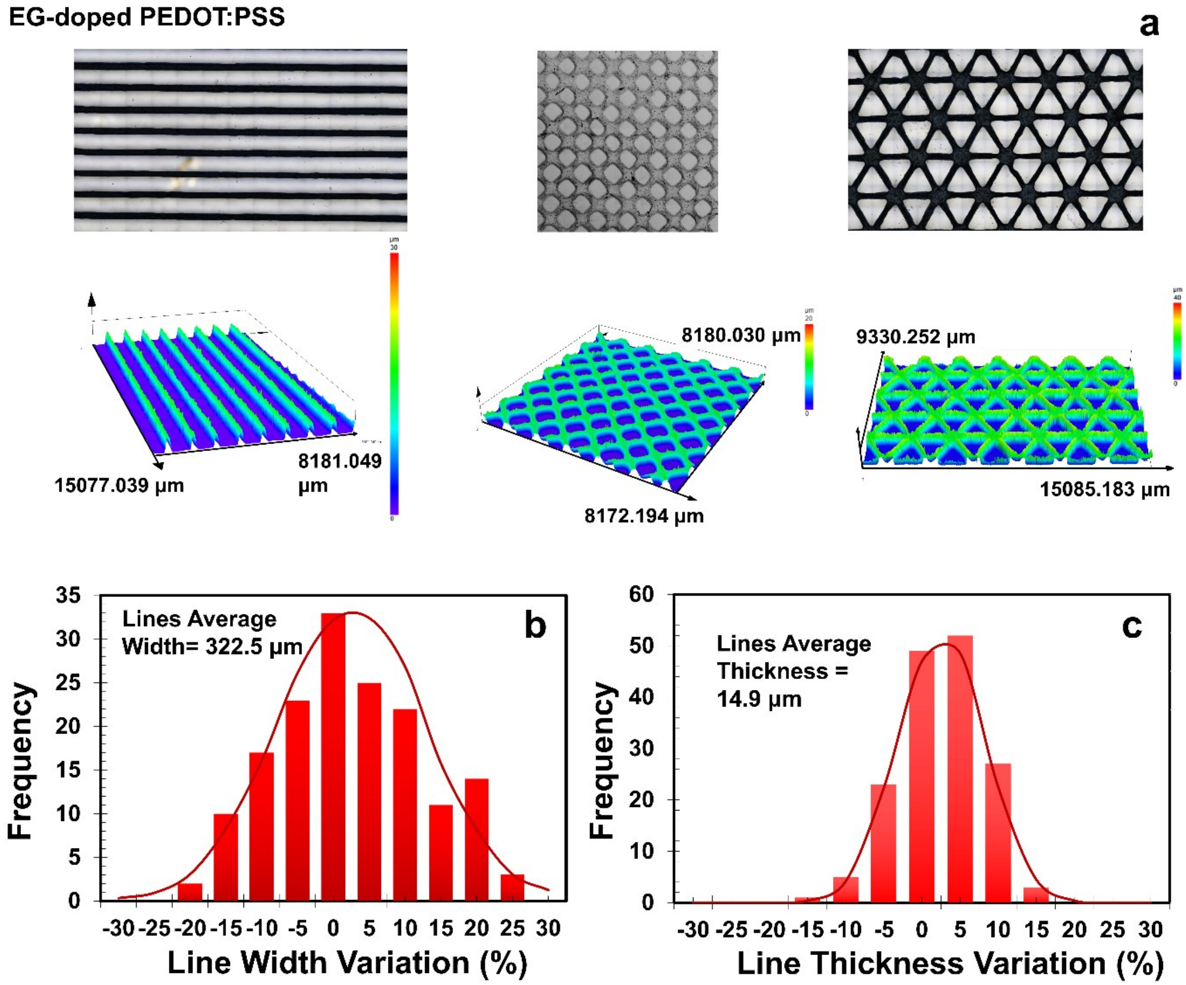

Figure S9. Topographical micrographs of line-, grid-, and triangle-patterned structures of EG-doped 6 wt.% PEDOT:PSS ink (a), statistical analysis of line width variation (b) and line thickness variation (c) of the printed EG-doped 6 wt.% PEDOT:PSS lines.

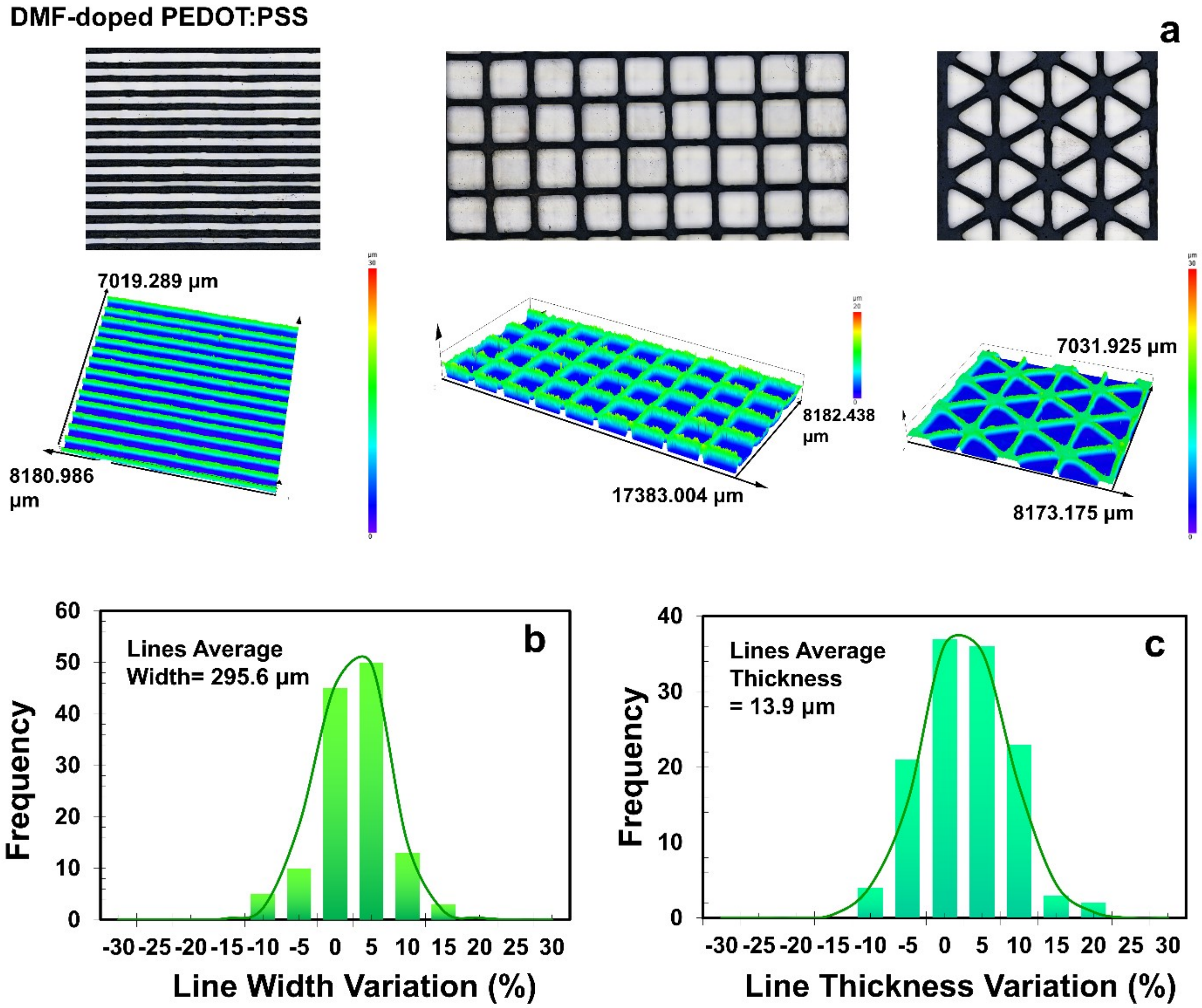

Figure S10. Topographical micrographs of line-, grid-, and triangle-patterned structures of DMF-doped 6 wt.% PEDOT:PSS ink (a), statistical analysis of line width variation (b) and line thickness variation (c) of the printed DMF-doped 6 wt.% PEDOT:PSS lines.

Table S1. Comparison of printing resolution of various 3D printing techniques.

Material	Co-solvent	Printing method	Resolution	Application	Ref.
PEDOT:PSS	EG	DIW	> 620 μm	Micro-supercapacitors	1
PEDOT:PSS	-	DIW	> 200 μm	Li-ion batteries	2
PEDOT:PSS	DMSO	DIW	> 320 μm	Bio-Photoelectrochemical Cells	3
PEDOT:PSS	-	DIW	> 175 μm	Electrochemical transistors	4
PEDOT:PSS	DMSO	DIW	> 30 μm	Implantable patches	5
PEDOT:PSS	-	DIW	> 30 μm	Bioelectronic Devices	6
PEDOT:PSS	-	DIW	> 450 μm	Bioelectronics	7
PEDOT:PSS	PEO[1]	DIW	> 245 μm		8
PEDOT:PSS	PEO	eDIW[2]	> 64 μm		8
PEDOT:PSS	Ionic additives	Inkjet printing	> 40 μm	Field-effect transistor arrays	9
PEDOT:PSS	DMSO	Inkjet printing	> 44 μm	Touch sensor	10
PEDOT:PSS	-	Inkjet printing	> 50 μm	Transistor circuits	11
PEDOT:PSS	-	Screen printing	> 200 μm	Electrochemical transistors	12
PEDOT:PSS	-	Aerosol printing	> 500 μm	Strain sensor	13
PEDOT:PSS	-	Microlithography	> 360 μm	Bioelectronics	7
PEDOT:PSS	Ionic liquid	Lithographically	> 5 μm	Implantable microelectronics	14
PEDOT:PSS	DMSO	DIW	> 296 μm	EMI shielding	**This work**

[1] Polyethylene oxide

[2] Electrostatically-assisted direct ink writing

Table S2. Comparison of electrical conductivity of various co-solvent treated PEDOT:PSS films.

Filler	**Conductivity (S cm^{-1})**	**Method of processing**	**Ref.**
Water	3	Spin coating	15
DMSO	1.75	Spin coating	16
	73	Spin coating	17
	130	Inkjet printing	18
	80	Casting	19
	600	Casting	20
	670.5	Spin coating	21
	1980	Spin coating	22
	437	Spin coating	23
	619	Spin coating	24
Dimethyl sulfate	132	Spin coating	25
EG	1.3	Spin coating	16
	160	Spin coating	26
	200	Spin coating	27
	1000	Spin coating	22
	242	Casting	28
	274.5	Spin coating	29
	621.6	Casting	30
	960	Spin coating	15
	640	Spin coating	31
	735	Spin coating	32
Polyethylene glycol	890	Spin coating	15
DMF	30	Casting	19
	1.2	Spin coating	15
Tetrahydrofuran	4	Casting	19
Methanol	370	Spin coating	15
	50.5	Spin coating	33
Ethanol	46	Spin coating	33
Glycerol	450	Inkjet printing	34
Sorbitol	10	Spin coating	35
	118.3	Spin coating	36
	100	Spin coating	37
Methoxyethanol	0.61	Spin coating	38
Diethylene glycol	10	Spin coating	39
Meso-erythritol	155	Spin coating	40
Xylitol	115	Casting	41
DMSO (doped)	858.1	Casting	**This work**
EG (doped)	652.3	Casting	**This work**
DMF (doped)	492.8	Casting	
DMSO (post-treated)	967	Casting	
EG (post-treated)	801.8	Casting	
DMF (post-treated)	828.6	Casting	
Methanol (post-treated)	813.8	Casting	
Ethanol(post-treated)	445	Casting	

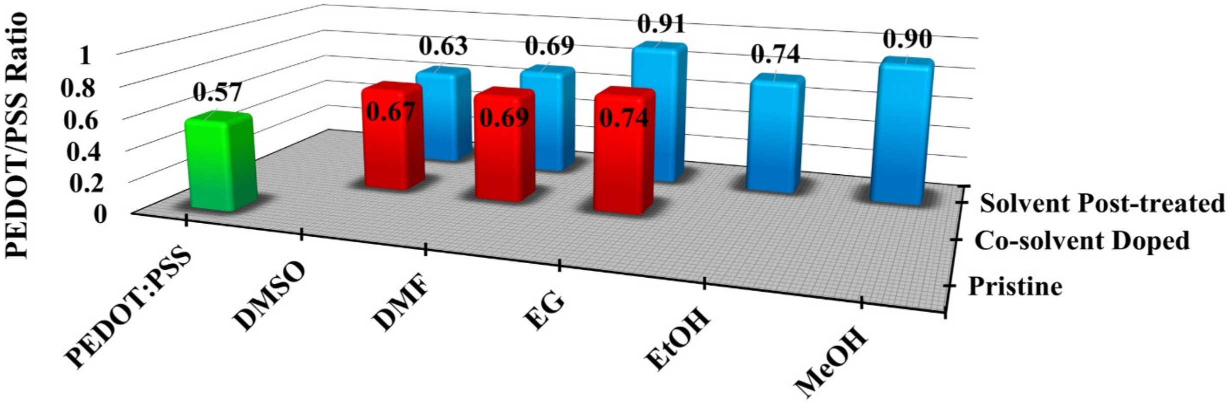

Figure S11. The PEDOT/PSS ratio was calculated from the surface areas under the XPS spectra for PEDOT (~165 eV) and PSS (~169 eV) characteristic peaks. The solvent treatment confirms the partial PSS removal form and increases the ratio of PEDOT to PSS, as a result, enhancing the electrical conductivity.

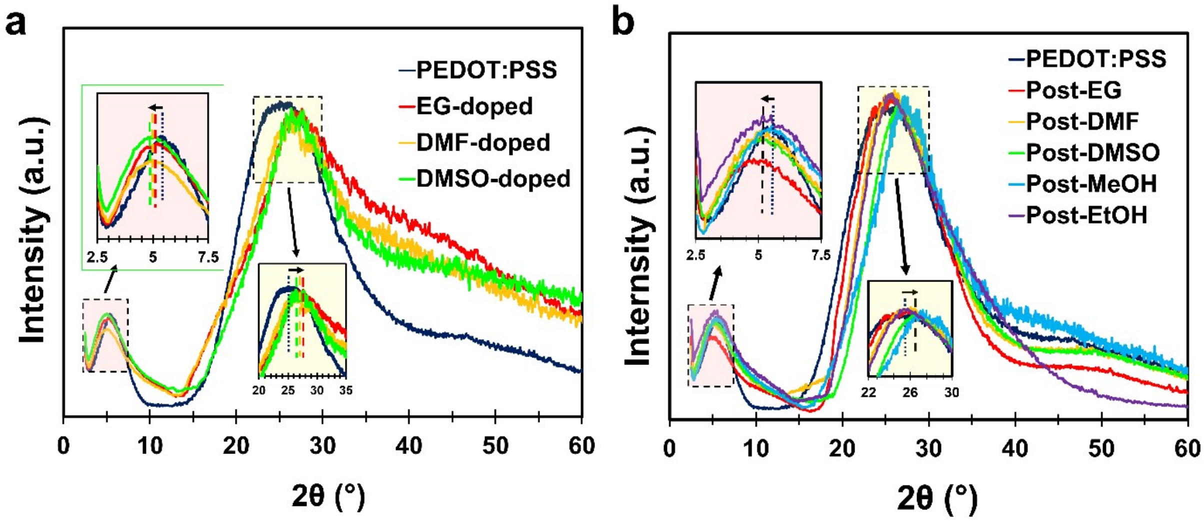

Figure S12. XRD spectra for co-solvent doped (a) and solvent post-treated (b) PEDOT:PSS films.

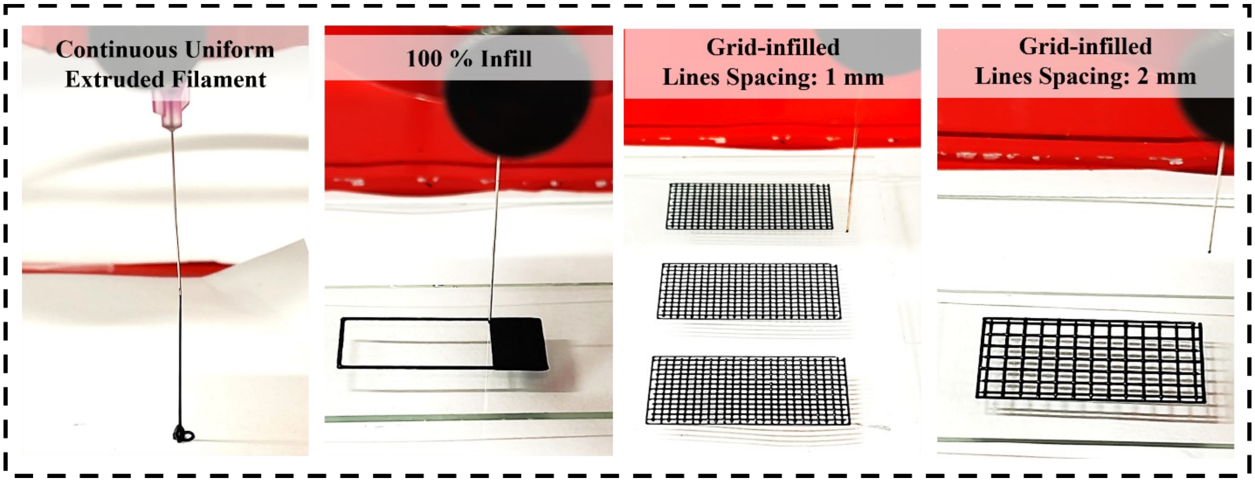

Figure S13. DIW printed structures with different infill densities.

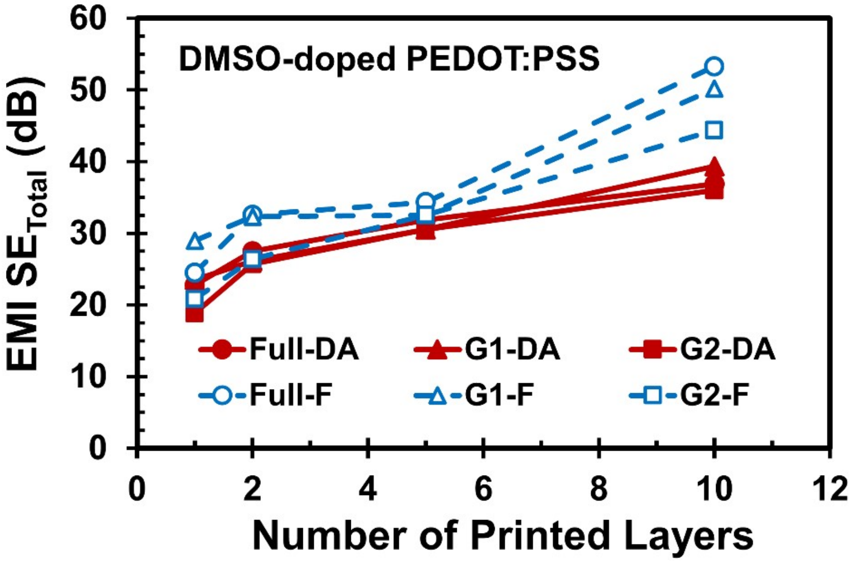

Figure S14. EMI SE$_{Total}$ of the printed structures as a function of the number of printed layers.

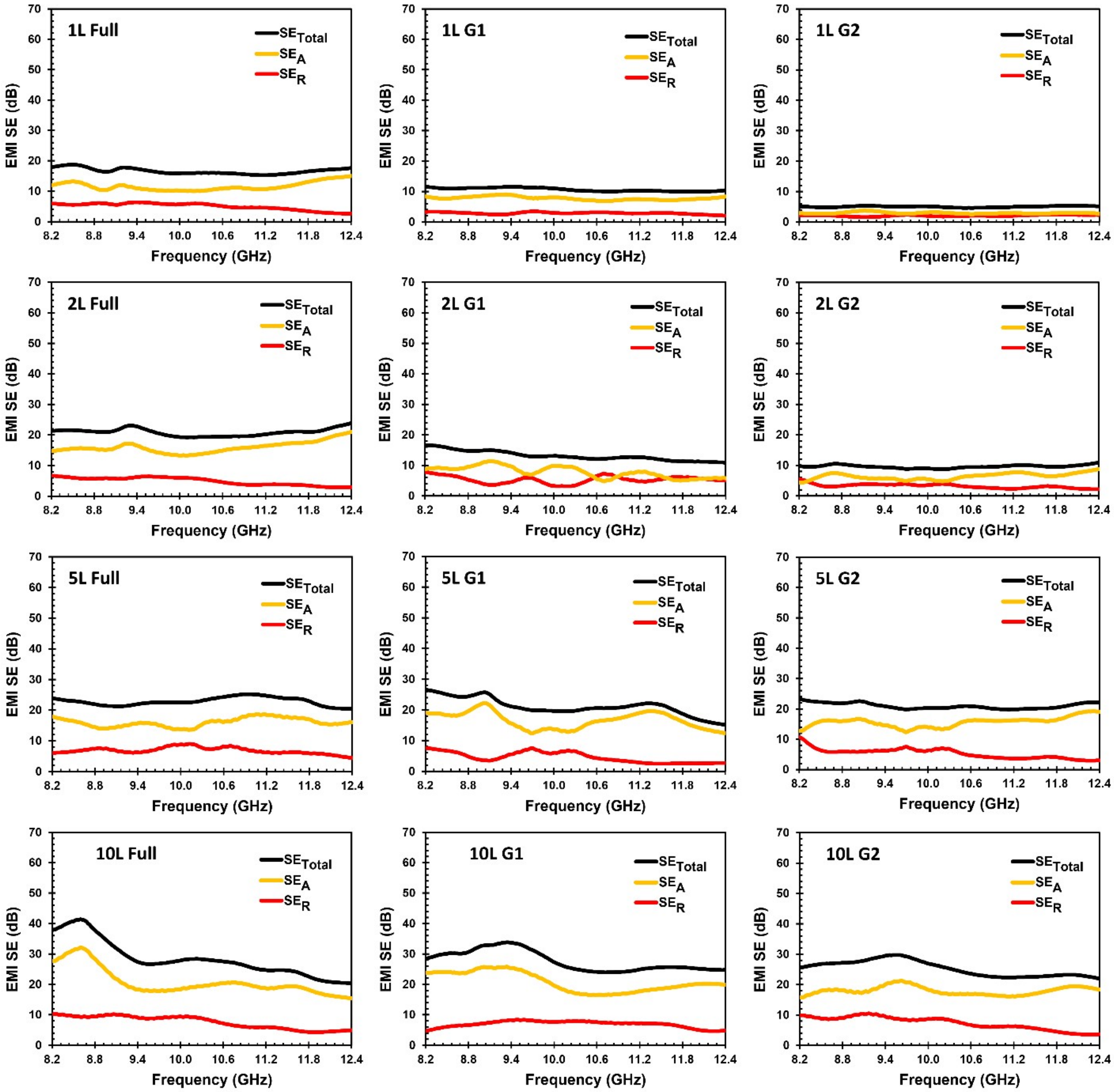

Figure S15. EMI SE of the printed structures of pristine 6 wt.% PEDOT:PSS over the X-band frequency range (8.2-12.4 GHz).

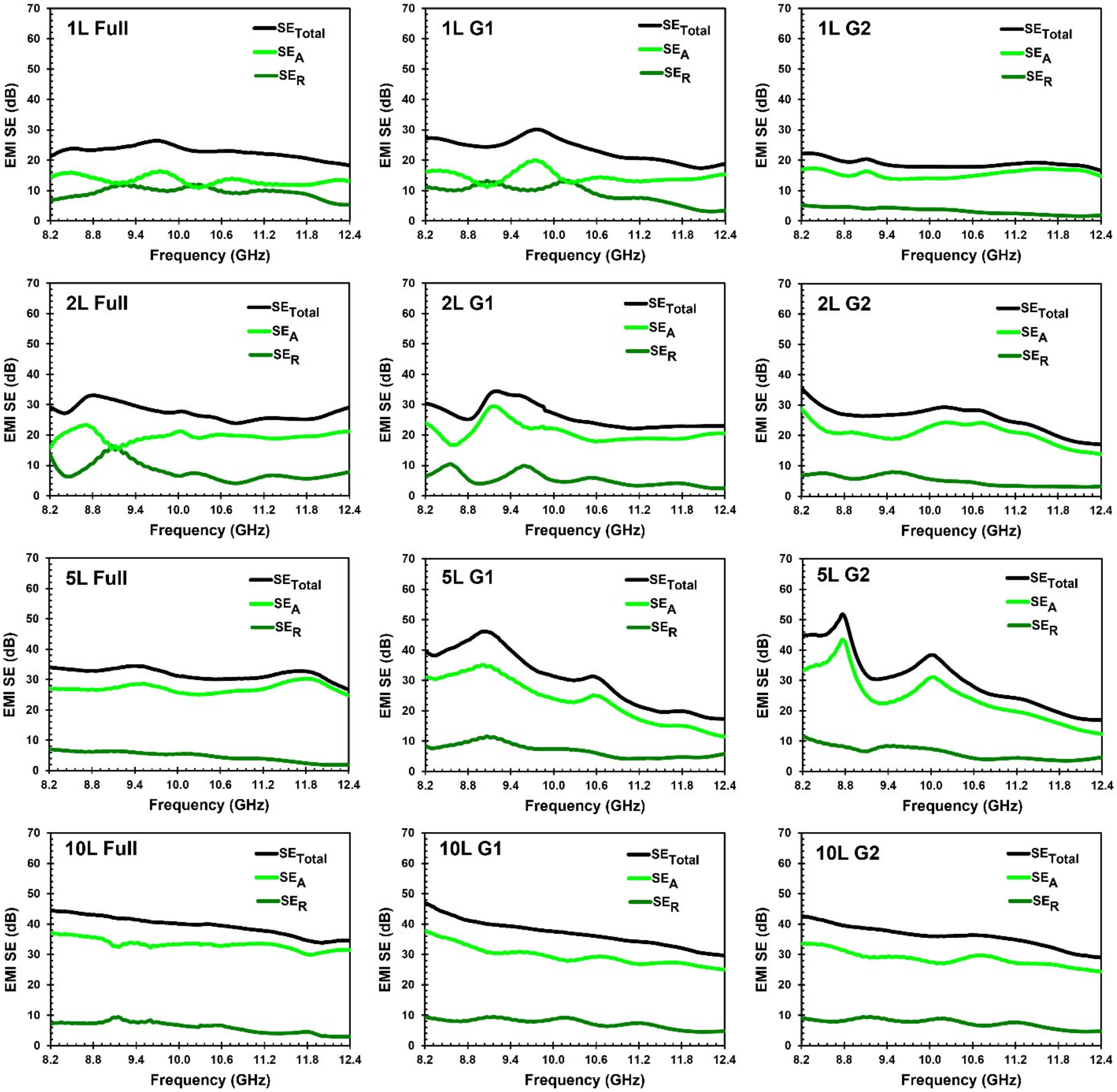

Figure S16. EMI SE of the printed structures of dry-annealed 3D-printed DMSO-doped 6 wt.% PEDOT:PSS over the X-band frequency range (8.2-12.4 GHz).

s

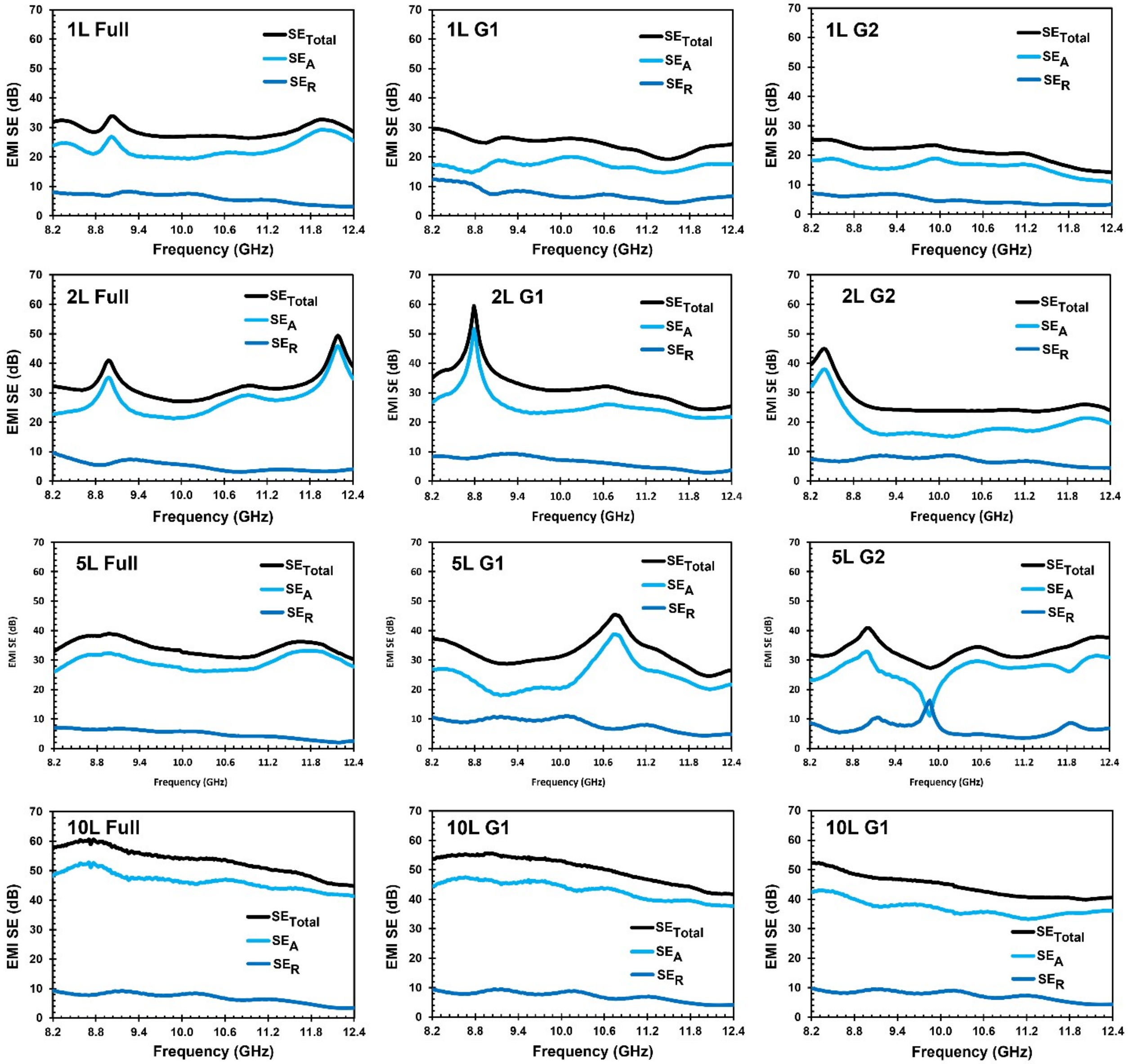

Figure S17. EMI SE of the printed structures of freeze-dried 3D-printed DMSO-doped 6 wt.% PEDOT:PSS over the X-band frequency range (8.2-12.4 GHz).

Table S3. Comparison of electrical conductivity and conductivity EMI shielding parameters for different materials.

EMI Shielding Material		Thickness (mm)	Conductivity (S cm^{-1})	SE$_{Total}$ (dB)	SSE/t (dB cm^2 g^{-1})	Reference
PEDOT:PSS/ Graphene		0.8	6.84	70	841	42
		1.5	22.3	69.1	8040	43
		1.5	35.2	91.9	20800	43
PEDOT:PSS/ $Ti_2C_3T_x$		0.011	340.5	42.1	19498	44
		0.06	388	41	89924	45
		0.007	2900	55.4	38079	46
		5	0.02	32.5	5000	47
		5	0.03	59	10841	47
PEDOT:PSS/ Ti_2C_3		0.021	1600	28.06	32240	48
		0.024	100	16.26	20246	48
PEDOT:PSS/PVA/Ag NWs		0.020	3.82	33.6	16800	49
PEDOT:PSS/WPU		0.15	77	62	4590	50
Dry-annealed DMSO-doped PEDOT:PSS	1L Full	0.0094	858.1	22.78	69251.05	**This work**
	1L G1	0.0080		21.50	209558.95	
	1L G2	0.0080		18.87	306505.52	
	2L Full	0.0271		27.49	27587.05	
	2L G1	0.0149		26.14	126564.86	
	2L G2	0.0149		25.70	213279.60	
	5L Full	0.0433		31.84	19239.11	
	5L G1	0.0331		30.55	64356.92	
	5L G2	0.0331		30.54	111984.78	
	10L Full	0.1967		39.36	4876.05	
	10L G1	0.1842		36.91	13458.56	
	10L G2	0.1842		35.99	23216.06	
Freeze-dried DMSO-doped PEDOT:PSS	1L Full	0.0167	858.1	28.95	90564.40	**This work**
	1L G1	0.0113		24.48	339972.76	
	1L G2	0.0113		20.81	481754.05	
	2L Full	0.0453		32.57	36782.22	
	2L G1	0.0331		32.31	142623.97	
	2L G2	0.0331		26.38	199616.42	
	5L Full	0.3908		34.34	4411.93	
	5L G1	0.3523		32.53	13019.08	
	5L G2	0.3523		32.90	22921.02	
	10L Full	0.6128		53.30	4284.72	
	10L G1	0.5014		50.16	13581.82	
	10L G2	0.5014		44.37	21257.80	

References

1 L. Li, J. Meng, X. Bao, Y. Huang, X. Yan, H. Qian, C. Zhang and T. Liu, *Adv Energy Mater*, 2023, 2203683.

2 P. Bao, Y. Lu, P. Tao, B. Liu, J. Li and X. Cui, *Ionics (Kiel)*, 2021, **27**, 2857–2865.

3 Y. J. Kim, S. Il Kim, J. Kim, J. Yun, H. Hong, J. Kim and W. Ryu, *ACS Appl Energy Mater*, 2023, **6**, 773–781.

4 J. Fan, C. Montemagno and M. Gupta, *Org Electron*, 2019, **73**, 122–129.

5 H. Yuk, B. Lu, S. Lin, K. Qu, J. Xu, J. Luo and X. Zhao, *Nat Commun*, 2020, **11**, 1–8.

6 Y. Zheng, Y. Wang, F. Zhang, S. Zhang, K. D. Piatkevich, N. Zhou and J. K. Pokorski, *Adv Mater Technol*, 2022, **7**, 2101514.

7 J. R. Aggas, S. Abasi, J. F. Phipps, D. A. Podstawczyk and A. Guiseppi-Elie, *Biosens Bioelectron*, 2020, **168**, 112568.

8 X. Wang, J. Plog, K. M. Lichade, A. L. Yarin and Y. Pan, *J Manuf Sci Eng*, 2023, **145**, 011008.

9 Y. Wang, C. Zhu, R. Pfattner, H. Yan, L. Jin, S. Chen, F. Molina-Lopez, F. Lissel, J. Liu, N. I. Rabiah, Z. Chen, J. W. Chung, C. Linder, M. F. Toney, B. Murmann and Z. Bao, *Sci Adv*, 2023, **3**, e1602076.

10 I. Basak, G. Nowicki, B. Ruttens, D. Desta, J. Prooth, M. Jose, S. Nagels, H.-G. Boyen, J. D'Haen and M. Buntinx, *Polymers (Basel)*, 2020, **12**, 2915.

11 H. Sirringhaus, T. Kawase, R. H. Friend, T. Shimoda, M. Inbasekaran, W. Wu and E. P. Woo, *Science (1979)*, 2000, **290**, 2123–2126.

12 P. Andersson Ersman, R. Lassnig, J. Strandberg, D. Tu, V. Keshmiri, R. Forchheimer, S. Fabiano, G. Gustafsson and M. Berggren, *Nat Commun*, 2019, **10**, 5053.

13 B. Thompson and H.-S. Yoon, *IEEE Sens J*, 2013, **13**, 4256–4263.

14 Y. Liu, J. Liu, S. Chen, T. Lei, Y. Kim, S. Niu, H. Wang, X. Wang, A. M. Foudeh, J. B.-H. Tok and Z. Bao, *Nat Biomed Eng*, 2019, **3**, 58–68.

15 Z. Yu, Y. Xia, D. Du and J. Ouyang, *ACS Appl Mater Interfaces*, 2016, **8**, 11629–11638.

16 O. P. Dimitriev, D. A. Grinko, Y. V Noskov, N. A. Ogurtsov and A. A. Pud, *Synth Met*, 2009, **159**, 2237–2239.

17 I. Cruz-Cruz, M. Reyes-Reyes, M. A. Aguilar-Frutis, A. G. Rodriguez and R. López-Sandoval, *Synth Met*, 2010, **160**, 1501–1506.

18 P. Wilson, C. Lekakou and J. F. Watts, *Org Electron*, 2013, **14**, 3277–3285.

19 J. Y. Kim, J. H. Jung, D. E. Lee and J. Joo, *Synth Met*, 2002, **126**, 311–316.

20 M. Hokazono, H. Anno and N. Toshima, *J Electron Mater*, 2014, **43**, 2196–2201.

21 K. Lim, S. Jung, S. Lee, J. Heo, J. Park, J.-W. Kang, Y.-C. Kang and D.-G. Kim, *Org Electron*, 2014, **15**, 1849–1855.

22 E. Hosseini, V. O. Kollath and K. Karan, *J. Mater. Chem. C*, 2020, **8**, 3982–3990.

23 Z. Zhu, C. Liu, J. Xu, Q. Jiang, H. Shi and E. Liu, *Electronic Materials Letters*, 2016, **12**, 54–58.

24 C. Yi, A. Wilhite, L. Zhang, R. Hu, S. S. C. Chuang, J. Zheng and X. Gong, *ACS Appl Mater Interfaces*, 2015, **7**, 8984–8989.

25 M. Reyes-Reyes, I. Cruz-Cruz and R. López-Sandoval, *The Journal of Physical Chemistry C*, 2010, **114**, 20220–20224.

26 J. Ouyang, C. Chu, F. Chen, Q. Xu and Y. Yang, *Adv Funct Mater*, 2005, **15**, 203–208.

27 J. Ouyang, Q. Xu, C.-W. Chu, Y. Yang, G. Li and J. Shinar, *Polymer (Guildf)*, 2004, **45**, 8443–8450.

28 C. Liu, B. Lu, J. Yan, J. Xu, R. Yue, Z. Zhu, S. Zhou, X. Hu, Z. Zhang and P. Chen, *Synth Met*, 2010, **160**, 2481–2485.

29 V. Singh, S. Arora, M. Arora, V. Sharma and R. P. Tandon, *Semicond Sci Technol*, 2014, **29**, 045020.

30 W. Wichiansee and A. Sirivat, *Materials Science and Engineering: C*, 2009, **29**, 78–84.

31 D. A. Mengistie, P.-C. Wang and C.-W. Chu, *J Mater Chem A Mater*, 2013, **1**, 9907–9915.

32 Y. H. Kim, C. Sachse, M. L. Machala, C. May, L. Müller-Meskamp and K. Leo, *Adv. Funct. Mater.*, 2011, **21**, 1076–1081.

33 S.-P. Rwei, Y.-H. Lee, J.-W. Shiu, R. Sasikumar and U.-T. Shyr, *Polymers (Basel)*, 2019, **11**, 134.

34 M.-W. Lee, M.-Y. Lee, J.-C. Choi, J.-S. Park and C.-K. Song, *Org Electron*, 2010, **11**, 854–859.

35 A. M. Nardes and M. Kemerink, *Org. Electron*, 2008, **9**, 727.

36 A. Onorato, M. A. Invernale, I. D. Berghorn, C. Pavlik, G. A. Sotzing and M. B. Smith, *Synth Met*, 2010, **160**, 2284–2289.

37 S. Timpanaro, M. Kemerink, F. J. Touwslager, M. M. De Kok and S. Schrader, *Chem Phys Lett*, 2004, **394**, 339–343.

38 Z. Hu, J. Zhang and Y. Zhu, *Renew Energy*, 2014, **62**, 100–105.

39 X. Crispin, F. L. E. Jakobsson, A. Crispin, P. C. M. Grim, P. Andersson, A. v Volodin, C. Van Haesendonck, M. Van der Auweraer, W. R. Salaneck and M. Berggren, *Chemistry of Materials*, 2006, **18**, 4354–4360.

40 J. Ouyang, C. Chu, F. Chen, Q. Xu and Y. Yang, *Adv Funct Mater*, 2005, **15**, 203–208.

41 Y. Li, R. Tanigawa and H. Okuzaki, *Smart Mater Struct*, 2014, **23**, 074010.

42 N. Agnihotri, K. Chakrabarti and A. De, *RSC Adv*, 2015, **5**, 43765–43771.

43 Y. Wu, Z. Wang, X. Liu, X. Shen, Q. Zheng, Q. Xue and J.-K. Kim, *ACS Appl Mater Interfaces*, 2017, **9**, 9059–9069.

44 R. Liu, M. Miao, Y. Li, J. Zhang, S. Cao and X. Feng, *ACS Appl Mater Interfaces*, 2018, **10**, 44787–44795.

45 P. J. Bora, A. G. Anil, P. C. Ramamurthy and D. Q. Tan, *Mater Adv*, 2020, **1**, 177–183.

46 A. Ghaffarkhah, M. Kamkar, H. Riazi, E. Hosseini, Z. A. Dijvejin, K. Golovin, M. Soroush and M. Arjmand, *New Journal of Chemistry*, 2021, **45**, 20787–20799.

47 G.-Y. Yang, S.-Z. Wang, H.-T. Sun, X.-M. Yao, C.-B. Li, Y.-J. Li and J.-J. Jiang, *ACS Appl Mater Interfaces*, 2021, **13**, 57521–57531.

48 A. Ghaffarkhah, M. Kamkar, Z. A. Dijvejin, H. Riazi, S. Ghaderi, K. Golovin, M. Soroush and M. Arjmand, *Carbon N Y*, 2022, **191**, 277–289.

49 J. Yu, W. Gu, H. Zhao and G. Ji, *Sci China Mater*, 2021, **64**, 1723–1732.

50 P. Li, D. Du, L. Guo, Y. Guo and J. Ouyang, *J Mater Chem C Mater*, 2016, **4**, 6525–6532.